Check for updates

RESEARCH ARTICLE

NANO · MICRO small
www.small-journal.com

Fast Near-Infrared Photodetectors Based on Nontoxic and Solution-Processable $AgBiS_2$

Yi-Teng Huang, Davide Nodari, Francesco Furlan, Youcheng Zhang, Marin Rusu, Linjie Dai, Zahra Andaji-Garmaroudi, Daniel Darvill, Xiaoyu Guo, Martina Rimmele, Thomas Unold, Martin Heeney, Samuel D. Stranks, Henning Sirringhaus, Akshay Rao, Nicola Gasparini, and Robert L. Z. Hoye**

Solution-processable near-infrared (NIR) photodetectors are urgently needed for a wide range of next-generation electronics, including sensors, optical communications and bioimaging. However, it is rare to find photodetectors with >300 kHz cut-off frequencies, especially in the NIR region, and many of the emerging inorganic materials explored are comprised of toxic elements, such as lead. Herein, solution-processed $AgBiS_2$ photodetectors with high cut-off frequencies under both white light (>1 MHz) and NIR (approaching 500 kHz) illumination are developed. These high cut-off frequencies are due to the short transit distances of charge-carriers in the ultrathin photoactive layer of $AgBiS_2$ photodetectors, which arise from the strong light absorption of this material, such that film thicknesses well below 120 nm are sufficient to absorb >65% of NIR to visible light. It is also revealed that ion migration plays a critical role in the photo-response speed of these devices, and its detrimental effects can be mitigated by finely tuning the thickness of the photoactive layer, which is important for achieving low dark current densities as well. These outstanding characteristics enable the realization of air-stable, real-time heartbeat sensors based on NIR $AgBiS_2$ photodetectors, which strongly motivates their future integration in high-throughput systems.

1. Introduction

Near-infrared photodetectors (NIR PDs) have been gaining increasing attention over the past decade, owing to the increasing needs in automotive vehicles, smart phones, augmented reality, machine vision, biometric monitoring, and imaging.[1–4] Many high throughput applications, such as optical communication[5] and computed axial tomography,[6] also require NIR PDs with fast photo-response. The speed of the photo-response of PDs is usually characterized by the cut-off frequency ($f_{-3\,dB}$), which is highly associated with the rise and fall times of PDs under pulsed light excitation.

In the wavelength range between 850–1100 nm, which is crucial for LiDAR (light detection and ranging) technology[7] and biomedical imaging,[8,9] silicon-based PDs dominate the current market due to their low cost and easy integration. However, silicon-based PDs are usually bulky

Y.-T. Huang, X. Guo, R. L. Z. Hoye
Inorganic Chemistry Laboratory
Department of Chemistry
University of Oxford
South Parks Road, Oxford OX1 3QR, UK
E-mail: robert.hoye@chem.ox.ac.uk

Y.-T. Huang, Y. Zhang, L. Dai, Z. Andaji-Garmaroudi, S. D. Stranks, H. Sirringhaus, A. Rao
Cavendish Laboratory
University of Cambridge
JJ Thomson Ave, Cambridge CB3 0HE, UK

D. Nodari, F. Furlan, M. Heeney, N. Gasparini
Department of Chemistry and Centre for Processable Electronics
Imperial College London
White City Campus
London W12 0BZ, UK
E-mail: n.gasparini@imperial.ac.uk

M. Rusu, T. Unold
Struktur und Dynamik von Energiematerialien
Helmholtz-Zentrum Berlin für Materialien und Energie
14109 Berlin, Germany

D. Darvill, R. L. Z. Hoye
Department of Materials
Imperial College London
Exhibition Road, London SW7 2AZ, UK

M. Rimmele, M. Heeney
KAUST Solar Center, Physical Science and Engineering Division
King Abdullah University of Science and Technology
Thuwal 23955-6900, Saudi Arabia

S. D. Stranks
Department of Chemical Engineering and Biotechnology
University of Cambridge
Philippa Fawcett Drive, Cambridge CB3 0AS, UK

The ORCID identification number(s) for the author(s) of this article can be found under https://doi.org/10.1002/smll.202310199

© 2023 The Authors. Small published by Wiley-VCH GmbH. This is an open access article under the terms of the Creative Commons Attribution License, which permits use, distribution and reproduction in any medium, provided the original work is properly cited.

DOI: 10.1002/smll.202310199

and require sophisticated manufacturing processes, making them less attractive as portable or wearable devices. On the other hand, organic materials,[10–12] lead-halide perovskites,[7,13] and chalcogenide quantum dots (QDs)[14–16] have demonstrated higher absorption coefficients in the NIR region than silicon, and their solution processability at low temperatures enables them to be compatible with polymer substrates, which are ideal for flexible and lightweight electronics. Nevertheless, NIR PDs based on these materials also face various challenges. For example, the performance of NIR organic PDs is limited either by the low charge-carrier mobility or high non-radiative recombination losses,[17] while perovskite PDs are not stable in air and encapsulation is usually needed. Additionally, heavy metal contamination to the environment (e.g., Pb or Cd pollution) remains a concern for PDs based on metal-halide perovskites (e.g., Pb-Sn perovskites) and chalcogenide QDs (e.g., PbS and CdTe QDs) used for NIR photodetection. Indeed, the usage of Pb and Cd in consumer electronics is regulated in many jurisdictions, such as by the EU Restriction of Hazardous Substances (RoHS) directive to up to 0.1 wt.% for Pb and 0.01 wt.% for Cd.[18] Apart from these challenges, another limiting factor is that very few of the above solution-processed PDs could achieve cut-off frequencies exceeding 300 kHz under visible light illumination, and it is even rarer in the NIR region (Table S1, Supporting Information). So far, to our knowledge, cut-off frequencies exceeding 300 kHz in the NIR region have only been reported in PDs based on toxic PbS QDs and a small handful of organic materials.[19,20] The limited options for fast, solution-processable NIR PDs could be a potential hindrance in high-speed applications, such as optical communication and data transfer.

$AgBiS_2$ is composed of RoHS-compliant elements with sufficient availability for commercial applications.[21] It has emerged as a promising absorber for photovoltaics, especially due to its high absorption coefficients exceeding those of conventional inorganic thin film materials.[22–24] As a result, efficient photovoltaics are achievable using only 30 nm thick absorber layers.[23] Surprisingly, although the bandgap of $AgBiS_2$ (≈1.0–1.3 eV) is also suitable for NIR light detection, there are very few investigations into $AgBiS_2$ NIR PDs. Some early studies have demonstrated that a high cut-off frequency in the visible region (630 nm wavelength) and a high specific detectivity D^* in the NIR region could be achieved in PDs based on solution-processed bulk thin films of $AgBiS_2$[25] and $AgBiS_2$ nanocrystals (NCs),[26,27] respectively (Table S1, Supporting Information). Nevertheless, $AgBiS_2$ PDs that simultaneously exhibit outstanding photodetection along with a fast response in the NIR range have not yet been realized. It is important to note that fast responses in the UV or visible wavelength ranges cannot guarantee the same performance in the NIR range, as recently shown by Kang et al.[27]

With escalating demand for ultrafast NIR technology over the past decade, developing cost-effective, high-performance and solution-processable NIR PDs that are fully compliant with regulations for consumer electronics are urgently needed. In this work, we develop PDs that fully address these requirements based on colloidal $AgBiS_2$ NCs. We hypothesized that the thickness of the photoactive layer is a critical parameter to achieve optimal performance. Thus, we finely tuned the NC film thickness through layer-by-layer (LBL) deposition from 20 to 115 nm and determined the effect on the external quantum efficiency, dark current density and noise current. Having established devices giving high responsivities and specific detectivities, we sought to understand the influence of thickness on the response speed of the PDs under white light or NIR (940 nm wavelength) illumination. We rationalized the results obtained by analyzing the drift lengths, transient responses, and transit times. From these measurements, we identified ion migration as a hidden factor affecting the transient response of $AgBiS_2$ PDs. Furthermore, we quantified the activation energy barrier for ion migration, and how it influences PD performance as a function of $AgBiS_2$ layer thickness. Finally, we demonstrated the practical applications of $AgBiS_2$ PDs by testing them as real-time heartbeat sensors operating without encapsulation in ambient air.

2. Results and Discussion

2.1. Photodetector Performance of $AgBiS_2$ PDs in the NIR Region

The $AgBiS_2$ NCs used in this work were synthesized through a modified hot-injection process[22] (see the Experimental Section for details), and they had a mean size of 4 ±1 nm (Figure S1a, Supporting Information). These $AgBiS_2$ NCs have a rocksalt crystal structure, with both Ag^+ and Bi^{3+} randomly occupying the same crystallographic lattice site. Drop-cast $AgBiS_2$ NCs could retain their phase and visual appearance in ambient air with relative humidity ranging from 60–70% for over a month (Figure S2, Supporting Information), suggesting their high air stability.

Herein, $AgBiS_2$ PDs were fabricated using an established *n-i-p* photodiode architecture[22,24] (**Figure 1a**), where ZnO and PTB7/MoO_x were adopted as the electron (ETL) and hole transport layers (HTL), respectively. The energy levels of the ETL and HTL were acquired from Kelvin probe (KP) and photoelectron yield spectroscopy (PYS) measurements[28] (Figure S12, Supporting Information). As displayed in Figure S12c (Supporting Information), although photo-excited holes could be extracted effectively, a small barrier might be present between $AgBiS_2$ and the ETL, which will be discussed in Section 2.4. Ligand exchange treatment with tetramethylammonium iodide (TMAI) in methanol solution enabled the use of the LBL method to fabricate PDs with controlled photoactive layer thickness (see details in the Experimental Section). A representative secondary electron microscopy (SEM) image of the cross-section of a complete PD is shown in Figure S3 (Supporting Information), where we can see the well-defined ETL, photoactive layer, and Ag electrode, verifying the uniformity of each layer over a large length scale. Our TMAI-treated $AgBiS_2$ films showed a bandgap of 1.2 eV (Figure S4b, Supporting Information) along with high absorption coefficients from the UV to NIR region, which exceeded 10^4 cm^{-1} for wavelengths below 1200 nm, and exceeded 10^5 cm^{-1} for wavelengths below 775 nm (Figure S4, Supporting Information), making them suitable for NIR photodetection.

To achieve high-performing PDs, the number of photoactive layers (i.e., TMAI-treated $AgBiS_2$ NC films) was tuned from 2 to 9 to reduce the dark current density J_D. Herein, J_D was only monitored at reverse biases smaller than 0.5 V (i.e., $-V_A \leq 0.5$ V). Although a larger reverse bias (−1–−10 V) is commonly used in commercial silicon PDs in order to extract charge-carriers out of their thick photoactive layers (hundreds of micrometers), it is not necessary for $AgBiS_2$ PDs because ultrathin photoactive

© 2023 The Authors. Small published by Wiley-VCH GmbH

16136829, 2024, 18, Downloaded from https://onlinelibrary.wiley.com/doi/10.1002/smll.202310199 by Helmholtz-Zentrum Berlin Für, Wiley Online Library on [28/04/2025]. See the Terms and Conditions (https://onlinelibrary.wiley.com/terms-and-conditions) on Wiley Online Library for rules of use; OA articles are governed by the applicable Creative Commons License

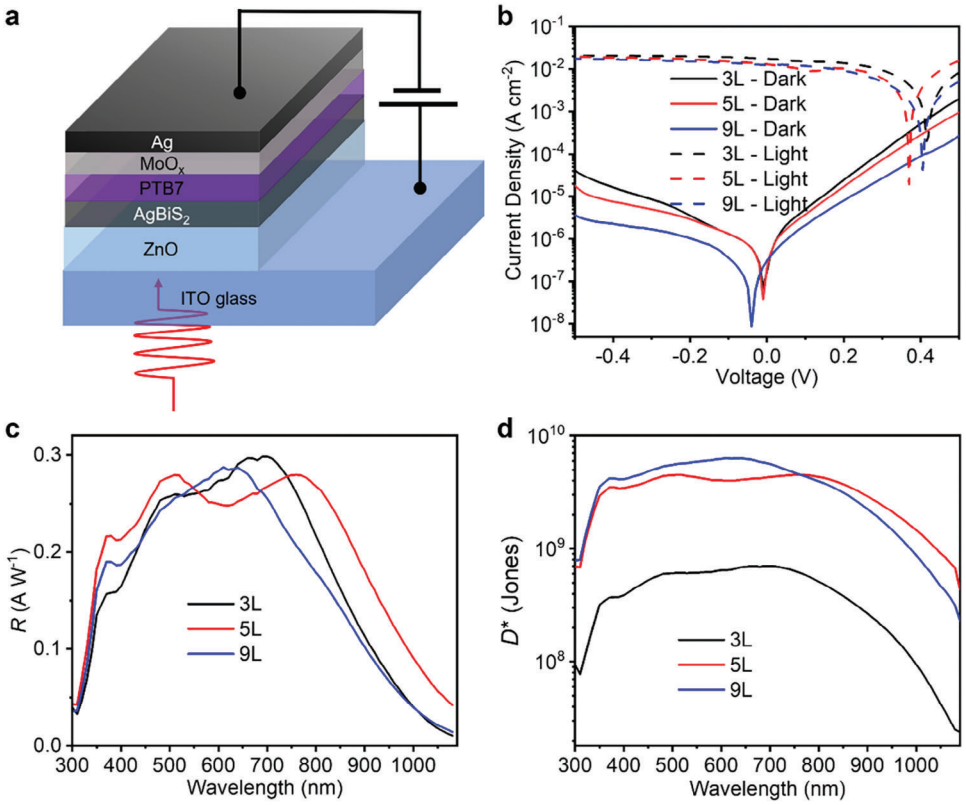


Figure 1. Performance of $AgBiS_2$ PDs. a) The *n-i-p* photodiode architecture of $AgBiS_2$ PDs. b) Dark current and photocurrent density under 1-sun illumination (AM1.5G spectrum) at different voltages. The dark current density - voltage (J_D–V) and photocurrent density - voltage (J_{ph}–V) curves arerepresented by the solid and dashed lines), respectively. c) Responsivity (R) and d) specific detectivity (D^*) spectra of $AgBiS_2$ PDs with 3 (3L), 5 (5L), and 9 (9L) photoactive layers. D^* was determined using the directly-measured noise currents. If these D^* values were instead calculated based on the Equation 1, as is common practice in the literature, they would be over an order of magnitude larger (Figure S8, Supporting Information).

layers (<120 nm) are sufficient for absorbing >65% of visible and near-infrared light (wavelengths <800 nm). Being able to operate these devices under smaller applied biases is advantageous for applications in wireless sensors as part of the Internet of Things, where reducing external power requirements is critical for these autonomous devices. The J_D–V curves of $AgBiS_2$ PDs with 2–9 photoactive layers deposited (denoted as 2L–9L) are shown in Figure S5a (Supporting Information), where we can see that there is an overall decrease in J_D with an increase in the number of the photoactive layers deposited. At the same time, $AgBiS_2$ PDs with different photoactive layers exhibited distinct external quantum efficiency (EQE) spectra (Figure S5b, Supporting Information), possibly caused by different optical interference effects. To compare the capability of these $AgBiS_2$ PDs in terms of NIR photodetection, the EQE values at 940 nm wavelength, and the J_D values at −0.5 V, are simultaneously shown in Figure S5c (Supporting Information), where we can clearly see that the highest EQE and the lowest J_D value, which are both desired for ideal NIR PDs, were not obtained from the same thickness of photoactive layer. Therefore, to investigate how the photoactive layer thickness affects PD performance, $AgBiS_2$ PDs with 3, 5, and 9 photoactive layers (denoted as the 3L, 5L, and 9L $AgBiS_2$ PD) were characterized in detail, as will be discussed below. We note that in order to make direct comparisons between these devices, the operational conditions used (i.e., light sources and applied biases) were all the same for these different measurements. Herein, 5L and 9L $AgBiS_2$ PDs account for the devices showing the highest EQE values in the NIR region and the lowest J_D, respectively, while 3L $AgBiS_2$ PDs account for the thinnest devices among the three types as a reference.

The representative current density–voltage (J–V) curves of the $AgBiS_2$ PDs in the dark and under 1-sun illumination are displayed in Figure 1b, where we can see a J_D value of 4.1×10^{-5}, 1.8×10^{-5}, and 0.37×10^{-5} A cm^{-2} at −0.5 V for the 3L, 5L, and 9L PD, respectively. This decrease in J_D with increasing $AgBiS_2$ NC film thickness was possibly caused by a decrease in shunt pathways. We therefore estimated the shunt resistance R_{shunt} of the devices from the reciprocals of the first derivative of the J_D–V curves at 0 V (Figure S6a, Supporting Information). Despite the large variation between devices, we could still observe an overall enhanced R_{shunt} in thicker PDs. As shown in Figure S6b (Supporting Information), the average R_{shunt} value of the 3L, 5L, and 9L PD is 0.22 ± 0.08, 0.61 ± 0.17, and 0.76 ± 0.17 MΩ cm^2, respectively. While we cannot make a like-for-like comparison in the J_D values with other reports due to the different measurement conditions used by different groups, the J_D values achieved with $AgBiS_2$ PDs at 0.5 V applied bias are within the range of strongly-performing NIR organic,[10,29] lead-halide perovskite[30,31] and PbS QD PDs[32,33] (see Table S1, Supporting Information). Figure 1c shows the responsivity (R)

© 2023 The Authors. Small published by Wiley-VCH GmbH

16136829, 2024, 18, Downloaded from https://onlinelibrary.wiley.com/doi/10.1002/smll.202310199 by Helmholtz-Zentrum Berlin Für, Wiley Online Library on [28/04/2025]. See the Terms and Conditions (https://onlinelibrary.wiley.com/terms-and-conditions) on Wiley Online Library for rules of use; OA articles are governed by the applicable Creative Commons License

spectra of these devices. Since R is proportional to the EQE value, it is not surprising that the 5L PD would display higher R values in the NIR region (750–1080 nm) with a peak value of 0.28 A W^{-1} at 770 nm.

Specific detectivity D^* is another important metric for PDs because it determines the signal-to-noise ratio of PDs, which is related to R by $D^* = \frac{\sqrt{AR}}{i_n}$ with A and i_n the photoactive area of the PD (4.5 mm^2), and the noise current spectral density, respectively. In the wider community, many researchers calculated i_n assuming it is only comprised of the shot and thermal noise, as defined by Equation 1.[34,35]

$$i_n = \sqrt{2qi_D + \frac{4kT}{R_{shunt}}} \quad (1)$$

In Equation 1, q is the elementary charge, i_D the static dark current, k the Boltzmann constant, T the temperature, and R_{shunt} the shunt resistance. In practice, other sources of noise could contribute to i_n as well. Therefore, using Equation 1, or even $\sqrt{2qi_D}$ only, which is also widely used in the literature,[32,36] would overestimate D^* values, as depicted in Figure S8 (Supporting Information). To avoid such an overestimation, we determined the i_n spectra of the devices by performing a Fast Fourier Transform (FFT) on the time evolution of the dark current (details in the Experimental Section). As shown in Figure S7a (Supporting Information), thicker devices tended to show lower i_n values, mainly due to their lower dark currents. The i_n spectra for all of the devices were invariant with frequency, indicating that flicker noise, which is usually ascribed to the random trapping and de-trapping processes,[37] does not play a significant role in these devices. The calculated i_n values based on Equation 1 for all devices are displayed as horizontal lines in Figure S7a (Supporting Information), and it can be seen that all of the measured i_n were at least an order of magnitude higher than the values calculated from Equation 1. This result again verifies the importance of direct noise current measurements for precise D^* determination. The tendency of the wider field working on solution-processed PDs to assume that the noise current only comes from shot noise, or a combination of shot and thermal noise, rather than directly measuring the noise current makes a comparison of D^* values between different reports difficult, with many previous reported values being over-estimated (see footnote to Table S1, Supporting Information).

The D^* spectra of $AgBiS_2$ PDs were determined by their R spectra and the directly-measured i_n values, as shown in Figure 1d. Herein, the i_n value was extracted from the high-frequency region (>1 kHz) of the i_n spectrum for each device biased at −0.5 V (Figure S7a, Supporting Information), which is estimated to be 8.9×10^{-11}, 1.3×10^{-11}, and 9.5×10^{-12} A $Hz^{-1/2}$ for the 3, 5, and 9L PD, respectively. The 9L PD showed the highest D^*, with values over 10^9 Jones in the region below 780 nm wavelength due to its lowest i_n value, which is consistent with the lowest J_D value occurring in the 9L PD. However, the higher R values in the NIR region of the 5L PD enabled it to exhibit the highest D^* values (between 7×10^8 and 4×10^9 Jones) for wavelengths > 780 nm. Additionally, the peak D^* values of each PD (at 710, 770, and 620 nm wavelength for the 3L, 5L, and 9L PD, respectively) calculated based on the i_n values at different frequencies are also displayed in Figure S7b (Supporting Information), where we can see that the D^* values are almost frequency-independent. This frequency independence further verifies the validity of the D^* values reported in our work.

The linear dynamic range (LDR) and film morphology were also characterized for our $AgBiS_2$ PDs. Under 940 nm wavelength illumination, the 3L, 5L, and 9L PDs biased at −0.2 V could reach LDR values of 52, 68, and 65 dB, respectively (Figure S9a, Supporting Information). The slight decrease in the LDR value for the 3L device mainly resulted from the increased J_D values, which determined the lower limit of LDR. On the other hand, the $AgBiS_2$ PDs biased at −0.5 V showed a slightly sub-linear variation in photocurrent with light intensity (Figure S9b, Supporting Information), making the acquired LDR values less reliable. Such sub-linearity is possibly affected by ion migration taking place in $AgBiS_2$, which will be discussed in Section 2.4.

In addition, the morphology of the TMAI-treated $AgBiS_2$ films with different thicknesses deposited on top of the ZnO layer was characterized by atomic force microscopy (AFM). As displayed in Figure S10 (Supporting Information), all of the $AgBiS_2$ films showed a compact surface with a small root-mean-square (RMS) roughness (3.7, 3.5, and 3.3 nm for the 3, 5, and 9L $AgBiS_2$ films, respectively). Although smaller roughness values might be observed in thicker films, we emphasize that the present roughness values achieved in all of the samples are comparable to or even smaller than those reported in PbS QD (≈0.5–5 nm),[38,39] organic (≈0.5–10 nm),[10,40] and lead-halide perovskite films (≈10–50 nm),[41–43] suggesting that film morphology is not limiting the performance of these devices.

2.2. Fast Photo-Response of $AgBiS_2$ PDs

Having realized $AgBiS_2$ PDs with strong performance, we focused on understanding their photo-response speed in the NIR region and under broad-band white light illumination. Herein, cut-off frequency f_{-3dB} was characterized by measuring the damping of the generated photocurrents (I_{freq}) from the $AgBiS_2$ PDs under illumination with varying modulation frequencies, as given by Equation 2.

$$\text{Damping} = 20 \times \log_{10}\left(\frac{I_{freq}}{I_0}\right) \quad (2)$$

In Equation 2, I_0 is the photocurrent measured under continuous-wave (CW) light illumination. As the damping of the photocurrent drops to −3 dB, the associated frequency is f_{-3dB}. **Figure 2a** displays the damping measurements for $AgBiS_2$ PDs excited by a 940 nm LED driven by sinusoidal voltages at different frequencies, where we can see the high f_{-3dB} values of 244, 496, and 399 kHz for the 3L, 5L, and 9L PDs, respectively. We note that when PDs are illuminated by visible or UV light, they usually display higher f_{-3dB} values,[25,30,31] which might be due to higher diffusion currents as higher excess charge-carrier densities are created near the surface or increased filling of traps due to the higher power densities achieved in the shorter wavelength range. Indeed, this was also the case for the $AgBiS_2$ PDs under white light (400–800 nm wavelength) illumination, where f_{-3dB} values could reach 1.20, 1.44, and 1.35 MHz for the 3L, 5L, and

© 2023 The Authors. Small published by Wiley-VCH GmbH

16136829, 2024, 18, Downloaded from https://onlinelibrary.wiley.com/doi/10.1002/smll.202310199 by Helmholtz-Zentrum Berlin Für, Wiley Online Library on [28/04/2025]. See the Terms and Conditions (https://onlinelibrary.wiley.com/terms-and-conditions) on Wiley Online Library for rules of use; OA articles are governed by the applicable Creative Commons License

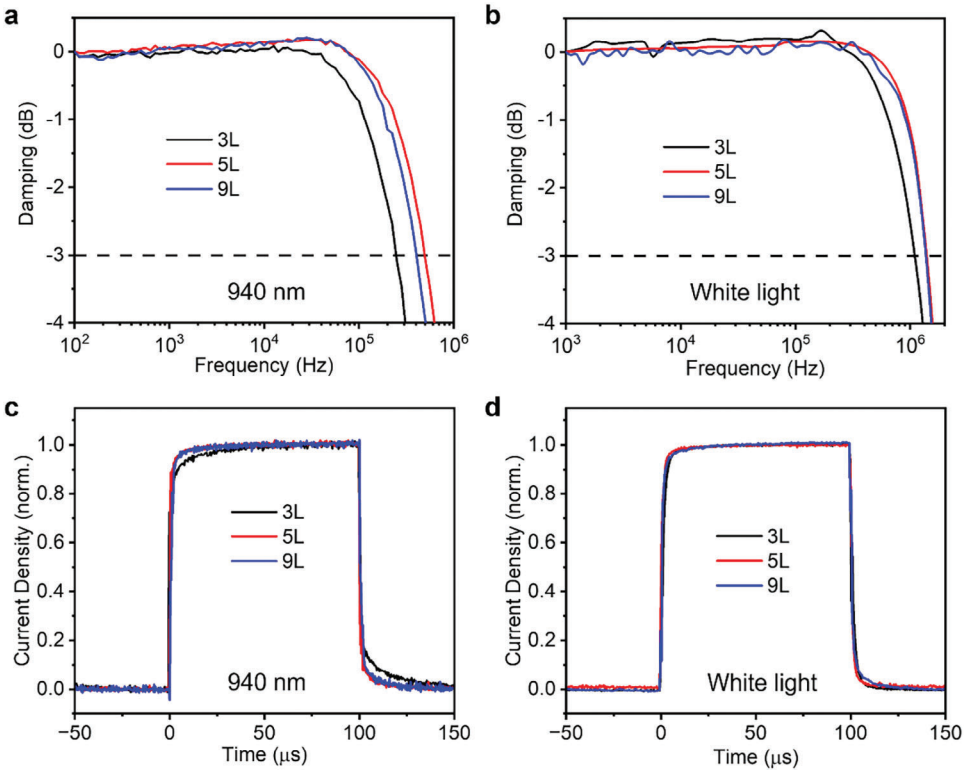


Figure 2. Fast response of $AgBiS_2$ PDs. Cut-off frequency measurements of the 3L, 5L, and 9L devices under illumination from a) 940 nm wavelength and b) white light LEDs driven by sinusoidal voltages at different frequencies. The normalized transient current densities of the 3L, 5L, and 9L devices under excitation from c) 940 nm wavelength and d) white light pulses emitted from LEDs. The pulse width was 100 μs for all the transient current density measurements. The devices were biased at 0 V in b) and at −0.5 V in other measurements.

9L devices, respectively. These cut-off frequencies are not only the highest values for $AgBiS_2$ PDs, but they also exceed most solution-processed NIR PDs, as can be seen in Table S1 (Supporting Information).

2.3. Rationalizing the Fast Response of $AgBiS_2$ PDs

It has been shown that the cut-off frequency f_{-3dB} can be associated with charge-carrier mobility and film thickness by Equation 3.[29]

$$f_{-3dB} \propto \frac{V\mu_e\mu_h}{d^2\left(\mu_e+\mu_h\right)} \tag{3}$$

In Equation 3, V is the applied voltage across the two electrodes of the photodiode, d the thickness of the photoactive layer, and μ_e and μ_h the electron and hole mobilities, respectively. In most solution-processed NIR PDs, d is at least a few hundreds of nanometers in order to achieve sufficient light absorption,[7,15,36] and their f_{-3dB} values would thus be limited by the long transit distances required. In addition, organic PDs suffer from low or unbalanced charge-carrier mobilities,[29,44] which could further lower their f_{-3dB} values, since charge-carrier transport will be limited by the smallest charge-carrier mobility. By contrast, the high absorption coefficients of $AgBiS_2$ NCs enable the fabrication of ultrathin devices here. As determined from AFM measurements, the $AgBiS_2$ film thicknesses in the 3L, 5L, and 9L PDs were only 19 ± 3, 38 ± 4, and 115 ± 9 nm, respectively. Furthermore, calculations also predicted the comparable effective masses of electrons and holes (the hole effective mass m_h* is approximately only double the electron effective mass m_e*)[45,46] in $AgBiS_2$, which could also be beneficial for achieving higher f_{-3dB} values by having relatively balanced electron and hole transport.

More importantly, the ultrathin photoactive layers could facilitate efficient charge-carrier extraction out of $AgBiS_2$ PDs. An estimate of the drift length L_{drift} can be obtained from the diffusion length $L_{diff} = \sqrt{D\tau}$, where D and τ are the diffusion constant and charge-carrier lifetimes, respectively. Since mobility μ can be associated with D by the Einstein relation, L_{drift} can be calculated using Equation 4.

$$L_{drift} = v_{drift}\,\tau = \mu\left(\frac{V}{d}\right)\tau = \frac{eD}{kT}\left(\frac{V}{d}\right)\tau = \frac{e}{kT}\left(\frac{V}{d}\right)L_{diff}^2 \tag{4}$$

In Equation 4, v_{drift} is the drift velocity. From time-resolved microwave conductivity (TRMC) measurements,[47] the electron and hole diffusion lengths of TMAI-treated $AgBiS_2$ NC films have been reported to be ≈60 and 150 nm, respectively.[47] Considering the $AgBiS_2$ PDs with different photoactive layers biased at −0.5 V, and assuming no screening of this field within the device, a L_{drift} value of at least 3516, 1758, and 611 nm (for holes) could be estimated for the 3L, 5L, and 9L devices, respectively. We can see that all of the L_{drift} values obtained from Equation 4 are

© 2023 The Authors. Small published by Wiley-VCH GmbH

16136829, 2024, 18, Downloaded from https://onlinelibrary.wiley.com/doi/10.1002/smll.202310199 by Helmholtz-Zentrum Berlin Für, Wiley Online Library on [28/04/2025]. See the Terms and Conditions (https://onlinelibrary.wiley.com/terms-and-conditions) on Wiley Online Library for rules of use; OA articles are governed by the applicable Creative Commons License

Table 1. The rise/fall time t_{rise}/t_{fall}, cut-off frequency f_{-3dB}, $1/R_tC$ values with R_tC the effective resistance-capacitance product, and estimated transit time t_{tr} of $AgBiS_2$ PDs.

Device	t_{rise}/t_{fall} [μs]	f_{-3dB} [Hz]	$1/R_tC$ [Ω^{-1} F^{-1}]	t_{tr} [μs]
3L	5.2/8.3(940 nm);3.7/3.6(white light)	244 k(940 nm);1.20 M(white light)	8.50×10^4	2.3 (940 nm);0.5 (white light)
5L	1.9/1.9(940 nm);2.6/2.5(white light)	496 k(940 nm);1.44 M(white light)	2.71×10^4	1.1 (940 nm);0.4 (white light)
9L	2.1/2.5(940 nm);3.0/3.7(white light)	399 k(940 nm);1.35 M(white light)	2.05×10^4	1.4 (940 nm);0.4 (white light)

substantially larger than the corresponding photoactive layer thicknesses in each device. Therefore, most photo-generated charge-carriers would be quickly swept across the photoactive layers under bias even in the thickest 9L $AgBiS_2$ PD. It has been reported in a PbS QD/metal Schottky diode, the response speed of the diode could be significantly improved when photo-generated charge-carriers were transported mainly by drift.[20] We note that a similar condition could be met in our $AgBiS_2$ PDs, where the thin photoactive layers were all included in the depletion regions so that drift transport would dominate and lead to a fast response.

The transient current densities of the $AgBiS_2$ PDs under pulsed illumination were measured to study their rise/fall times t_{rise}/t_{fall}. The normalized transient current dynamics of the 3L, 5L, and 9L PDs activated by light pulses emitted from a 940 nm and white light LED are displayed in Figure 2c,d, respectively. Here, the rise/fall times refer to the time required for the transient currents to rise from 10% to 90% of their maximum values, and drop from 90% to 10% of the maximum values, respectively. The acquired t_{rise}/t_{fall} values for the 3L, 5L, and 9L PDs are listed in **Table 1**, where we can see response times shorter than 10 μs in all of the devices under either 940 nm or white light illumination. In particular, the 5L PD showed the shortest t_{rise}/t_{fall} value of 1.9 μs out of all devices at 940 nm wavelength. Similar to the case of f_{-3dB} values, we emphasize that such a short t_{rise}/t_{fall} value is much more difficult to achieve in the NIR region compared to the visible region. In the visible region, although a short response time less than 1 μs has been reached in some $AgBiS_2$ PDs,[25,48] in the NIR region, only a fall time of 1.4 ms has been reported so far.[27] Therefore, the ultrafast photo-response in our $AgBiS_2$ PDs in the NIR region is very uncommon. The charge-carrier transit time t_{tr} through a PD can be estimated from Equation 5.[50]

$$t_{tr} = \frac{A_0}{\sqrt{\left(2\pi f_{-3dB}\right)^2 - \left(\frac{1}{R_tC}\right)^2}} \quad (5)$$

In Equation 5, A_0 is a constant typically equal to ≈3.5 and R_tC refers to the effective resistance-capacitance product of the overall experimental system. The series resistances of the $AgBiS_2$ PDs could be estimated from the reciprocals of the slopes of the photocurrent density–voltage curves (J_{ph}–V curves) at open-circuit (dashed lines in Figure 1b), and the effective resistance of the experimental system was then estimated by the summation of the series resistance of each device and the connected resistance within the oscilloscope (50 Ω). The C values were directly measured from the high-frequency range of the capacitance-frequency plots (Figure S11, Supporting Information). The R_tC values for different $AgBiS_2$ PDs are listed in Table 1, from which we can calculate the transit time t_{tr}.

As can be seen from Table 1, the calculated t_{tr} values were close to the t_{rise}/t_{fall} values under 940 nm light illumination, suggesting that the device response times were mainly determined by the charge-carrier transit times through the devices. On the other hand, under white light illumination, the t_{rise}/t_{fall} values tended to be slightly longer than the calculated t_{tr} values for each device. Indeed, smaller t_{rise}/t_{fall} values were initially expected to be reached under white light illumination (larger f_{-3dB} values) and also in thinner devices (larger drift velocities for charge-carriers), both of which were not the case, as can be seen from Table 1. These unusual phenomena along with the slightly sub-linear variation in photocurrent with illumination intensity when biased at −0.5 V (Figure S9b, Supporting Information) imply the influence of a hidden factor, ion migration, might occur in $AgBiS_2$ devices. Here, we propose that ion migration is facilitated by a stronger electric field (e.g., in thinner PDs or PDs biased at larger reverse voltages), or higher light intensity from the white light source, which could potentially induce a large charge-carrier gradient and hence drive ions migration more easily.[50,51] It is therefore important to understand the role of ion migration in $AgBiS_2$, which is examined in the next section.

2.4. Ion Migration in $AgBiS_2$

Ion migration has been observed in several perovskite and PbS QD-based devices,[53–54] where mobile cations or halide ligands could easily move when driven by the external electric field. In order to verify whether ion migration could also occur in $AgBiS_2$, temperature-dependent transient dark current measurements (see details in the Experimental Section) were performed here. At higher temperatures, more ions will be thermally activated[56] and accumulated near the electrodes, which would gradually screen the electric field between the two electrodes. As a result, the transient dark currents excited by voltage pulses would decay faster when the external field was screened more by the built-in field from the accumulated ions.

To simplify the analyses of ion migration in $AgBiS_2$, electron-only devices (architecture: ITO/ZnO/$AgBiS_2$/PCBM/Ag) with 3 photoactive layers (3L) were used here. An electron-only device was used because of the *n*-type nature of TMAI-treated $AgBiS_2$ films, as verified from KP and PYS measurements (Figure S12c, Supporting Information). **Figure 3a** shows the dark current transients of the electron-only $AgBiS_2$ device excited by high-voltage (4 V) pulses from 200 to 320 K, where we could indeed see the transients decaying faster at higher rates k_1 (Table S2, Supporting Information) as temperature was increased. The corresponding Arrhenius plot (analysis details in Note S1, Supporting Information) of $AgBiS_2$ is then displayed in Figure 3b, and an activation

© 2023 The Authors. Small published by Wiley-VCH GmbH

16136829, 2024, 18, Downloaded from https://onlinelibrary.wiley.com/doi/10.1002/smll.202310199 by Helmholtz-Zentrum Berlin Für, Wiley Online Library on [28/04/2025]. See the Terms and Conditions (https://onlinelibrary.wiley.com/terms-and-conditions) on Wiley Online Library for rules of use; OA articles are governed by the applicable Creative Commons License

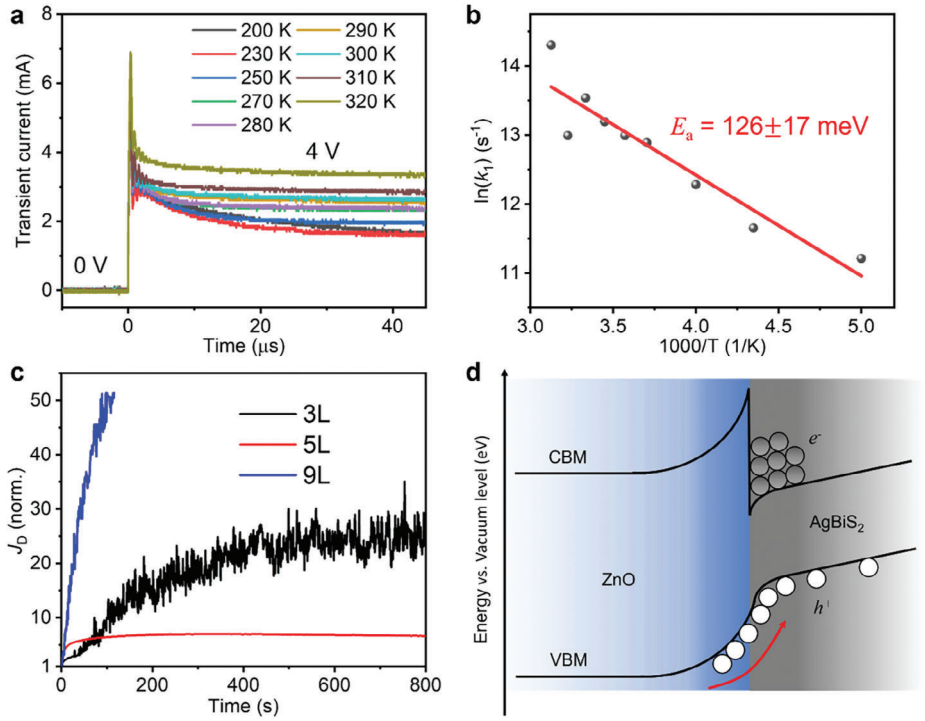


Figure 3. Understanding ion migration in $AgBiS_2$. a) Temperature-dependent transient dark currents of the electron-only 3L $AgBiS_2$ device (ITO/ZnO/$AgBiS_2$/PCBM/Ag) activated by voltage pulses (pulse height: 4 V, pulse width: 50 μs) from 200 to 320 K, and b) the corresponding Arrhenius plot, along with the extracted activation energy barrier, E_a. k_1, and T refer to the decay rate of the transient currents and temperature, respectively. c) Time evolution of the normalized dark current density J_D of the 3L, 5L, and 9L devices biased at −0.5 V. All the time evolution profiles were normalized to the initial J_D values at time = 0 s. d) Proposed band alignment and bending at the ZnO/$AgBiS_2$ heterojunction. CBM, VBM, e^- and h^+ refer to the conduction band minimum, valence band maximum, accumulated electrons, and injected holes, respectively.

energy barrier (E_a) of ≈126 ± 17 meV was extracted. This activation energy barrier is comparable to or smaller than those reported in lead-halide perovskites (typically in the range of 100–300 meV, with some reports of up to 600 meV[53,54,56,57]), where ion migration has been proven to strongly influence their device performance. We thus conclude here that ions could easily migrate in $AgBiS_2$ PDs, and possibly impact the photo-responses more significantly under a stronger electric field (e.g., in the 3L device) or higher light intensity[59] (e.g., under white light illumination).

To examine the possible impact of ion migration on the dark current density J_D of $AgBiS_2$ PDs over a longer time scale, we tracked the dark current density J_D of the 3L, 5L, and 9L $AgBiS_2$ PDs under continuous bias for a few minutes. As shown in Figure 3c, we noticed that the initial J_D value of the 3L and 5L devices were enhanced by a factor of 24 and 7, respectively, after 13 min, while the 9L device J_D was increased by a factor of 51 after only 2 min. Such an enhancement in J_D values suggests ion migration to occur in all the $AgBiS_2$ PDs biased over a long timescale. The accumulated ions at the $AgBiS_2$/transport layer interfaces could induce charge-injection from the electrodes, therefore leading to dark current drift. Such a J_D enhancement over long-term biasing was also observed in tetrabutylammonium iodide (TBAI)-treated PbS QDs,[60] and iodide anions have been claimed to be the main source for ion migration owing to their weaker binding energy with the PbS. Considering the similar crystal structure and iodide ligand used for $AgBiS_2$ films, iodide anions may also be the main source of migrating ions in $AgBiS_2$ PDs as well.

In addition, KP and PYS measurements indicated that the ZnO films used in this work had a lower electron affinity than the TMAI-treated $AgBiS_2$ film (Figure S12c, Supporting Information; i.e., negative conduction band offset). This could lead to a contact barrier (type-II heterojunction) at the ZnO/$AgBiS_2$ interface in these devices. Although some electrons may still tunnel through this barrier via the tail of states extending from the ZnO band edges[60] (which are also shown to be present from the broadband photoluminescence emission of the ZnO films; Figure S13, Supporting Information), they are more likely to accumulate at this heterointerface, which could encourage hole injection from ZnO under reverse bias, and hence increase the dark current, as displayed in Figure 3d.

Given that ions are driven by the application of an external field, thinner devices were expected to exhibit more significant ion migration, with a larger increase in J_D over time under continuous reverse bias. Therefore, it is not surprising to see a larger J_D enhancement and slower photo-response in the 3L device compared to the 5L device (Figure 3). Interestingly, although the 9L device had the smallest J_D at −0.5 V (Figure 1b), its J_D enhancement is still larger than other devices, suggesting that the applied field is not the only factor facilitating ion migration. As a result, the smallest J_D enhancement factor was actually seen from the 5L device. We proposed that such a small J_D increase could have benefited from 1) a smaller electric field compared to the

© 2023 The Authors. Small published by Wiley-VCH GmbH

16136829, 2024, 18, Downloaded from https://onlinelibrary.wiley.com/doi/10.1002/smll.202310199 by Helmholtz-Zentrum Berlin Für, Wiley Online Library on [28/04/2025]. See the Terms and Conditions (https://onlinelibrary.wiley.com/terms-and-conditions) on Wiley Online Library for rules of use; OA articles are governed by the applicable Creative Commons License

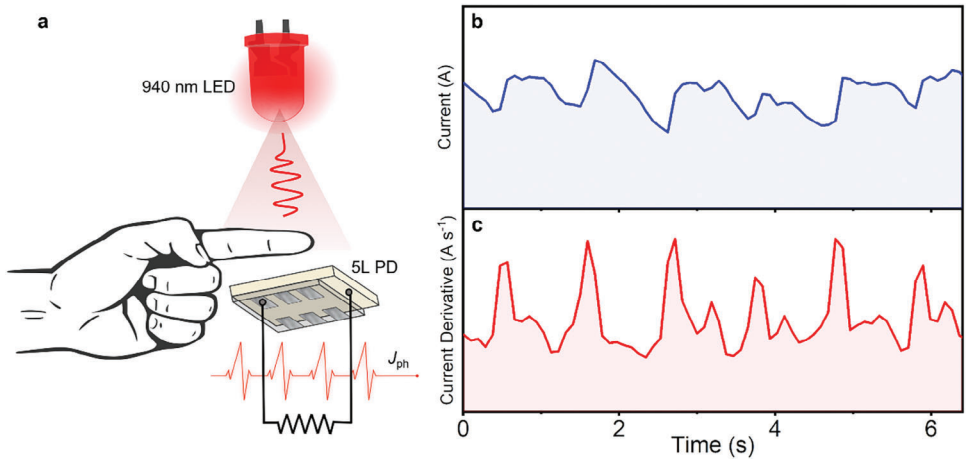


Figure 4. $AgBiS_2$ PDs as NIR heartbeat sensors. a) Schematic illustration of the real-time photoplethysmogram setup, and b) measurements of the heartbeat of a finger under 940 nm light illumination, along with c) its time derivative. The signals were recorded using the 5L $AgBiS_2$ PD.

3L device, and 2) a smaller number of defects introduced during the ligand-exchange process compared to the 9L device, which is further explained in Figure S14 (Supporting Information). The small J_D enhancement in the 5L device indicates the minor effect of ion migration in this device, which also contributes to its fastest photo-response (Figure 2).

Herein, we show that tuning the thickness of the photoactive layer is an effective strategy to achieve high shunt resistance while minimizing ion migration. The combination of these two factors is crucial for realizing strongly performing and fast NIR PDs. Increasing the number of layers deposited in the LBL process could lead to a larger shunt resistance, and hence lower J_D values. However, more defects are also introduced in thicker devices, which can be activated with the application of an electric field, facilitating ion migration. These mobile ions can accumulate via drift at the photoactive layer/transport layer interfaces, which could induce extra charge-carrier injection and result in dark current enhancement. As indicated above, the population of ions accumulated at these heterointerfaces is associated with both the strength of the electric field within the photoactive layer and the concentration of defects. Therefore, ion migration can be suppressed by fine-tuning the photoactive layer thickness in $AgBiS_2$ PDs to simultaneously reach a field strength and defect concentration as low as can be, as demonstrated in Figure S15 (Supporting Information). We note that although charge-carrier extraction is still efficient in all of our devices because of the thin photoactive layers, future efforts should focus on minimizing ion migration in order to achieve faster photo-responses. Based on the insights gained from this work, we also believe that reducing defects by using passivation agents and less polar solvents or changing the band alignment at the $AgBiS_2$/ZnO interface are important areas to target in future efforts.

2.5. Real-Time Heartbeat Monitoring Using $AgBiS_2$ PDs

To demonstrate the practical application of $AgBiS_2$ PDs, we performed real-time photoplethysmogram measurements using the 5L device. As shown in **Figure** 4a, the finger of a volunteer was placed between a 940 nm LED and a 5L $AgBiS_2$ PD. The pulsating bloodstream through the capillaries changed the transmission of 940 nm NIR light from an LED. In the NIR region, not only could light penetrate living tissue efficiently but also the difference in absorbance between oxygenated and deoxygenated hemoglobin will be maximized. As a result, the heartbeat rate of the volunteer could be precisely recorded as electrical signals by the 5L PD, as shown in Figure 4b. A clearer figure could be made when we differentiated the current signals with time (Figure 4c), where we could easily estimate a heartbeat rate of ≈60 beats per minute. Finally, it is worth mentioning that unlike lead-halide perovskite PDs, where J_D values might be enhanced by a factor of two after exposure to air for 10 days,[62] the J_D value of the unencapsulated $AgBiS_2$ PD was not increased when stored in an ambient environment (relative humidity: 60–70%) over 34 days (Figure S16, Supporting Information). The results here therefore strongly indicate the utility of $AgBiS_2$ in practical applications in air, and this could inspire future studies on using these fast PDs in high-throughput applications.

3. Conclusion

In this work, fast and air-stable NIR PDs that are comprised of fully RoHS-compliant elements have been realized by using $AgBiS_2$ NCs, and the electronic–ionic transport of the $AgBiS_2$ NC films was comprehensively studied. We showed that the fast response of these PDs comes about from the balanced charge-carrier transport and ultrathin photoactive layer, which benefits from the high absorption coefficients of cation-disordered $AgBiS_2$. Consequently, high $f_{-3\,dB}$ values over 1 MHz under white light illumination, and approaching 500 kHz in the NIR region, were achieved, which are higher than the values reported in previous reports of $AgBiS_2$ PDs as well as most solution-processed NIR PDs. At the same time, we found a small activation energy barrier of 126 meV in $AgBiS_2$ NC films, showing there to be facile ion migration, which limits how fast the photoresponse can be and leads to dark current drift. By carefully tuning the photoactive layer thickness, we could strike a balance between high shunt resistance, strength of the electric field in the

© 2023 The Authors. Small published by Wiley-VCH GmbH

16136829, 2024, 18, Downloaded from https://onlinelibrary.wiley.com/doi/10.1002/smll.202310199 by Helmholtz-Zentrum Berlin Für, Wiley Online Library on [28/04/2025]. See the Terms and Conditions (https://onlinelibrary.wiley.com/terms-and-conditions) on Wiley Online Library for rules of use; OA articles are governed by the applicable Creative Commons License

photoactive layer, and ion migration, leading to outstanding PD performance. Finally, $AgBiS_2$ PDs were demonstrated as heartbeat sensors under NIR illumination, which shows their great potential for practical applications, including for non-invasive diagnostics and optical communication, and this motivates future efforts on integrating $AgBiS_2$ in high-throughput applications. Our work therefore shows the benefits of these ultrathin light harvesters in terms of achieving high cut-off frequencies at a low reverse bias, which could be advantageous for applications in portable consumer electronics by reducing the requirements of the power supply unit.

4. Experimental Section

Synthesis of $AgBiS_2$ NCs: Bismuth acetate (99%, Alfa Aesar, 1mmol) and 0.8 mmol silver acetate (99.99%, Merck) were dissolved in 10 mL oleic acid (90%, Merck). The solution was degassed at 100 °C in a Schlenk line to remove oxygen and moisture for at least 2 h. The reaction atmosphere was then switched to an Ar line, and 1 mmol hexamethyldisilathiane (HMS) (Synthesis grade, Merck) dissolved in 5 mL 1-octadecene (ODE) (90%, Merck) was quickly injected into the degassed solution. The whole solution was heated at 100 °C under the Ar line for 20 min and then cooled down to room temperature in a water bath. The cooled-down solution was diluted by toluene (90%, Merck) and 1.5 times of acetone (90%, Merck) was added as the anti-solvent. The solution was then centrifuged at 5000 rpm for 3 min. The precipitated $AgBiS_2$ NCs were re-dispersed in toluene and the same purification process was repeated for another two times to ensure non-reacted precursors were completely removed. The purified $AgBiS_2$ NCs were dissolved in toluene and centrifuged at 3500 rpm for 3 min to precipitate larger NCs. The final NC solution was extracted after filtering the supernatant after the final centrifugation step by a 0.22 µm polytetrafluoroethylene (PTFE) filter.

Fabrication of $AgBiS_2$ PDs: ZnO sol–gel solution was prepared by dissolving 1 g zinc acetate (Merck, dihydrate) in 10 mL 2-methoxyethanol (>99%, Merck) and 284 µL ethanolamine (>99%, Merck). The ZnO ETLs were deposited by spin-coating the ZnO sol–gel solution at 3000 rpm for 30 s and heated at 200 °C for 10 min. 40 µL of 20 mg mL^{-1} $AgBiS_2$ NC solution with toluene as the solvent was spin-coated on ZnO at 2000 rpm for 35 s. 40 µL of 5 mg mL^{-1} TMAI (99%, Merck) solution with methanol as the solvent was dropped onto the $AgBiS_2$ film and kept there for 40 s to allow solid-state ligand exchange treatment to take place. During this treatment, the long-chain oleate ligands attaching to the surface of the $AgBiS_2$ NCs during synthesis were replaced by short-chain iodides, enabling more efficient charge-carrier transport between the NCs. Afterward, the TMAI-treated $AgBiS_2$ film was washed once individually by methanol and toluene at 2000 rpm for 35 s to remove the residual ligands. The effectiveness of ligand exchange was verified from the Fourier-transform Infrared (FTIR) absorbance spectra of pristine and TMAI-treated films (Figure S17, Supporting Information), where it could see a significant decrease in the intensity of the characteristic carboxylic peaks from oleate ligands in the latter, suggesting that most oleate ligands have been replaced. Thicker $AgBiS_2$ films could then be fabricated layer-by-layer by repeating the above processes (LBL process). Forty microliters of 5 mg mL^{-1} PTB7 (1-material) solution with 1,2-dichlorobenzene (99%, Merck) as the solvent was spin-coated at the $AgBiS_2$ films at 2000 rpm for 30 s. Finally, 3 nm MoO_x and 100 nm Ag were evaporated onto the PTB7 throughout a mask, which defined the device area of 4.5 mm^2. $AgBiS_2$ PDs were stored in air overnight before characterization.

Transmission Electron Microscopy (TEM) Measurements: TEM samples were prepared by putting a small drop of NC solution onto the carbon-coated copper grid. TEM images were recorded using FEI Tecnai F20 (200 kV).

Current Density–Voltage (J–V) Measurements: J_D–V curves were measured using a Keithley 4200 Source-Measure unit. To determine the linear dynamic range (LDR), a 940 nm wavelength LED, driven by a function generator (ThorLabs DC2200), was used. The LED light was attenuated using a selection of neutral density filters placed between the lamp and PDs. The photocurrent (J_{ph}) was calculated as the difference between the illuminated current density (J_{light}) and dark current density (J_D) at each light intensity. LDR values were calculated based on Equation 6:

$$\mathrm{LDR} = 20 \times \log_{10}\left(\frac{J_{max}}{J_{min}}\right) \tag{6}$$

where, J_{max} and J_{min} are J_{ph} values at the upper and lower limit of the linear region in a J_{ph}–light intensity curve.

Noise Current (i_n) Measurements: The i_n was extracted from the dark current density recorded by a digital oscilloscope (Siglent SDS6054A) with a current amplifier, followed by a fast Fourier transform (FFT).

Responsivity (R) Characterization: R values were measured using an integrated system from Quantum Design PV300.

Transient Current Measurements: Transient current measurements were performed using a digital oscilloscope (Siglent SDS6054A). The PDs were illuminated by either 940 nm or white light LEDs driven by a function generator (ThorLabs DC2200). For determination of the rise and fall time, a series of 5 kHz square voltage pulses were applied to the LEDs using the function generator. For determination of the cut-off frequency, sinusoidal functions with varying frequencies between 100 Hz and 2 MHz were used to drive the LEDs.

Photoplethysmography Measurements: Photoplethysmography measurements were performed by directly connecting the PDs to a Keithley 4200 Source-Measure unit and recording the current as a function of time upon illumination with 940 nm LED driven by a function generator (ThorLabs DC2200).

Impedance Spectroscopy: To record the impedance signal, a STAT-I-400 potentiostat of Metrohm LTD was used. The signal was measured starting from 1 MHz down to 1 Hz over 50 frequency points, using a potential amplitude of 20 mV, under 100 mW cm^{-2} at open-circuit voltage.

Temperature-Dependent Transient Current Measurements: Square voltage pulses with a voltage amplitude of 4 V and a time width of 50 µs were generated by a function generator (Hewlett Packard 8116A) and applied to the electron-only device connected in series with a resistor (330 Ω). The transient voltage across the resistor could be probed by an oscilloscope (RS PRO RSDS1304CFL) and transferred into a transient current. The device was mounted in a Desert TTP4 Probe Station system, which could control the temperature range from 150 to 360 K via an integrated cryostat in a high vacuum (10^{-6} mBar). At each temperature, devices were measured after being placed in the Probe Station system for at least 15 min in order to reach thermal equilibrium.

Kelvin Probe (KP) and Photoelectron Yield Spectroscopy (PYS) Measurements: Kelvin probe and photoelectron yield spectroscopy were combined[28] to measure the work function (Φ) and ionization energy (E_i), respectively, of the prepared thin films by employing a KP Technology SKP5050-APS02 setup under N_2 ambient. The KP system used a 2 mm-diameter tip with a gold alloy coating which was calibrated on a gold reference sample. The KP was placed in a Faraday cage to screen the external electrical fields. The work function was determined by measuring the contact potential difference (CPD) between the KP tip (reference electrode) with a known work function, Φ_{tip}, and the investigated thin film. The PYS setup uses the same KP to detect the photoemission currents as a function of incident photon energy. The light source comprised of a deuterium lamp coupled with a grating monochromator. The range of the incident photon energy was 3.4–7.5 eV. The sample was illuminated by a deep-UV optical fiber. The ionization energy, E_i, of samples was determined by measuring the photoelectron yield $Y(h\nu)$ as a function of photon energy $h\nu$. $Y(h\nu)$ is defined as the number of photoemitted electrons per incident photon at a given photon energy $h\nu$. By extrapolating the linear part of the $Y^{1/3}(h\nu)$–$h\nu$ plot, the ionization energy was estimated according to:

$$Y(h\nu) \propto (h\nu - E_i)^3 \tag{7}$$

© 2023 The Authors. Small published by Wiley-VCH GmbH

16136829, 2024, 18, Downloaded from https://onlinelibrary.wiley.com/doi/10.1002/smll.202310199 by Helmholtz-Zentrum Berlin Für, Wiley Online Library on [28/04/2025]. See the Terms and Conditions (https://onlinelibrary.wiley.com/terms-and-conditions) on Wiley Online Library for rules of use; OA articles are governed by the applicable Creative Commons License

Secondary Electron Microscopy (SEM) Imaging: SEM sample cross sections were cleaved and fixed upright into the chamber. SEM images were recorded using a Gemini 1 Zeiss Sigma 300 with an accelerating voltage of 5 keV.

Atomic Force Microscopy (AFM) Imaging: AFM measurements were conducted using an Agilent Technologies 5500 AFM in tapping mode. Images were analyzed using Gwyddion software.

Supporting Information

Supporting Information is available from the Wiley Online Library or from the author.

Acknowledgements

Y.-T.H. would like to thank the Ministry of Education, Taiwan and Downing College Cambridge for funding. N.G. and F.F. would like to acknowledge support from European Commission Research Executive Agency (Grant Agreement Number: 859752 HEL4CHIR-OLED H2020-MSCA-ITN-2019). L.D. thanks the Cambridge Trusts and the China Scholarship Council for funding. Y.-T.H. and R.L.Z.H. acknowledge support from the Silverman Research Fellowship, Downing College Cambridge. S.D.S. acknowledges the Royal Society and Tata Group (no. UF150033) for funding. The work received funding from the European Research Council under the European Union's Horizon 20202 research and innovation programme (HYPERION, no. 756962). R.L.Z.H. would like to thank EPSRC for financial support (grant no. EP/V014498/2), as well as the Royal Academy of Engineering through the Research Fellowships scheme (no. RF\201718\17101). M.H. would like to thank EPSRC (no. EP/T028513/1).

Conflict of Interest

The authors declare no conflict of interest.

Author Contributions

Y.-T.H. and D.N. contributed equally to this work. Y.-T.H., N.G., and R.L.Z.H. conceived of this work. Y.-T.H. developed and optimized the synthesis of $AgBiS_2$ NCs, fabricated $AgBiS_2$ devices, and performed XRD, FTIR, stability tests as well as temperature-dependent transient current measurements under the supervision of A.R. and R.L.Z.H. D.N. and F.F. performed PD characterization under the supervision of N.G. Y.Z. assisted the temperature-dependent transient current measurements under the supervision of H.S. M. Rusu and X.G. performed the KP and PYS measurements, under the supervision of T.U. and R.L.Z.H., respectively. L.D. took the TEM images under the supervision of S.D.S. Z.A.-G. performed the PDS measurements. D.D. helped with the cross-sectional SEM measurements. M. Rimmele helped with the AFM measurements, under the supervision of M.H. All authors discussed the results and wrote the paper together.

Data Availability Statement

The data accompanying this paper and the supporting information is available open access from the Oxford Research Repository under the DOI: 10.5287/ora-010ynqeyr. http://dx.doi.org/10.5287/ora-010ynqeyr.

Keywords

$AgBiS_2$, cut-off frequency, heart-beat sensors, near-infrared photodetectors, solution-processable electronics, ultrathin absorbers

Received: November 14, 2023
Revised: November 17, 2023
Published online: December 8, 2023

[1] S. Royo, M. Ballesta-Garcia, M. Ballesta-Garcia, *Appl. Sci.* **2019**, *9*, 4093.
[2] S. Park, K. Fukuda, M. Wang, C. Lee, T. Yokota, H. Jin, H. Jinno, H. Kimura, P. Zalar, N. Matsuhisa, S. Umezu, G. C. Bazan, T. Someya, *Adv. Mater.* **2018**, *30*, 1802359.
[3] M. BinLien, C. H. Liu, I. Y. Chun, S. Ravishankar, H. Nien, M. Zhou, J. A. Fessler, Z. Zhong, T. B. Norris, *Nat. Photonics* **2020**, *14*, 143.
[4] S. Inal, J. Rivnay, A.-O. Suiu, G. G. Malliaras, I. Mcculloch, *Acc. Chem. Res.* **2018**, *51*, 1368.
[5] E. H. Sargent, *Adv. Mater.* **2005**, *17*, 515.
[6] M. Babics, H. Bristow, W. Zhang, A. Wadsworth, M. Neophytou, N. Gasparini, I. Mcculloch, *J. Mater. Chem. C* **2021**, *9*, 2375.
[7] A. Morteza Najarian, M. Vafaie, A. Johnston, T. Zhu, M. Wei, M. I. Saidaminov, Y. Hou, S. Hoogland, F. P. García De Arquer, E. H. Sargent, *Nat. Electron.* **2022**, *5*, 511.
[8] E. Hemmer, A. Benayas, F. Légaré, F. Vetrone, *Nanoscale Horiz.* **2016**, *1*, 168.
[9] Z. Wu, Y. Zhai, H. Kim, J. D. Azoulay, T. N. Ng, *Acc. Chem. Res.* **2018**, *51*, 3144.
[10] P. Jacoutot, A. D. Scaccabarozzi, T. Zhang, Z. Qiao, F. Aniés, M. Neophytou, H. Bristow, R. Kumar, M. Moser, A. D. Nega, A. Schiza, A. Dimitrakopoulou-Strauss, V. G. Gregoriou, T. D. Anthopoulos, M. Heeney, I. Mcculloch, A. A. Bakulin, C. L. Chochos, N. Gasparini, *Small* **2022**, *18*, 2200580.
[11] W. Yang, W. Qiu, E. Georgitzikis, E. Simoen, J. Serron, J. Lee, I. Lieberman, D. Cheyns, P. Malinowski, J. Genoe, H. Chen, P. Heremans, *ACS Appl. Mater. Interfaces* **2021**, *13*, 16766.
[12] J. Huang, J. Lee, J. Vollbrecht, V. V. Brus, A. L. Dixon, D. X. Cao, Z. Zhu, Z. Du, H. Wang, K. Cho, G. C. Bazan, T.-Q. Nguyen, *Adv. Mater.* **2020**, *32*, 1906027.
[13] R. Ollearo, J. Wang, M. J. Dyson, C. H. L. Weijtens, M. Fattori, B. T. Van Gorkom, A. J. J. M. Van Breemen, S. C. J. Meskers, R. A. J. Janssen, G. H. Gelinck, *Nat. Commun.* **2021**, *12*, 7277.
[14] Q. Xu, I. T. Cheong, H. Song, V. Van, J. G. C. Veinot, X. Wang, *ACS Photonics* **2022**, *9*, 2792.
[15] I. Ka, L. F. Gerlein, I. M. Asuo, S. Bouzidi, D. M. Gedamu, A. Pignolet, F. Rosei, R. Nechache, S. G. Cloutier, *ACS Photonics* **2020**, *7*, 1628.
[16] M. Amiri, N. Alizadeh, *Mater. Sci. Semicond. Process.* **2020**, *111*, 104964.
[17] S. Gielen, C. Kaiser, F. Verstraeten, J. Kublitski, J. Benduhn, D. Spoltore, P. Verstappen, W. Maes, P. Meredith, A. Armin, K. Vandewal, *Adv. Mater.* **2020**, *32*, 2003818.
[18] RoHS, https://environment.ec.europa.eu/topics/waste-and-recycling/rohs-directive_en (accessed: August 2022).
[19] B.-H. Jiang, F.-C. Hsiao, Y.-R. Lin, C.-H. Lin, Y. A. Shen, Y.-Y. Hsu, P.-H. Lee, Y.-W. Su, H.-R. Lu, C.-W. Lin, C. K. Chan, C.-P. Chen, *ACS Appl. Mater. Interfaces* **2023**, *15*, 10907.
[20] J. P. Clifford, G. Konstantatos, K. W. Johnston, S. Hoogland, L. Levina, E. H. Sargent, *Nat. Nanotechnol.* **2009**, *4*, 40.
[21] U.S. Geological Survey, *Mineral Commodity Summaries 2023*, **2023**, https://doi.org/10.3133/mcs2023.
[22] M. Bernechea, N. Cates, G. Xercavins, D. So, A. Stavrinadis, G. Konstantatos, *Nat. Photonics* **2016**, *10*, 521.
[23] Y. Wang, S. R. Kavanagh, I. Burgués-Ceballos, A. Walsh, D. O. Scanlon, G. Konstantatos, *Nat. Photonics* **2022**, *16*, 235.
[24] C. Kim, I. Kozakci, J. Kim, S. Y. Lee, J. Y. Lee, *Adv. Energy Mater.* **2022**, *12*, 2200262.
[25] L. Jiang, Y. Li, J. Peng, L. Cui, R. Li, Y. Xu, W. Li, Y. Li, X. Tian, Q. Lin, *J. Mater. Chem. C* **2020**, *8*, 2436.
[26] I. Burgués-Ceballos, Y. Wang, G. Konstantatos, *Nanoscale* **2022**, *14*, 4987.
[27] J. Kang, J. T. Oh, H. Kim, H. Kim, H. Choi, I. H. Jung, *Appl. Surf. Sci.* **2022**, *597*, 153661.

© 2023 The Authors. Small published by Wiley-VCH GmbH

16136829, 2024, 18, Downloaded from https://onlinelibrary.wiley.com/doi/10.1002/smll.202310199 by Helmholtz-Zentrum Berlin Für, Wiley Online Library on [28/04/2025]. See the Terms and Conditions (https://onlinelibrary.wiley.com/terms-and-conditions) on Wiley Online Library for rules of use; OA articles are governed by the applicable Creative Commons License

[28] M. Rusu, T. Kodalle, L. Choubrac, N. Barreau, C. A. Kaufmann, R. Schlatmann, T. Unold, *ACS Appl. Mater. Interfaces* **2021**, *13*, 7745.
[29] S. Saggar, S. Sanderson, D. Gedefaw, X. Pan, B. Philippa, M. R. Andersson, S.-C. Lo, E. B. Namdas, *Adv. Funct. Mater.* **2021**, *31*, 2010661.
[30] H. L. Zhu, Z. Liang, Z. Huo, W. K. Ng, J. Mao, K. S. Wong, W.-J. Yin, W. C. H. Choy, *Adv. Funct. Mater.* **2018**, *28*, 1706068.
[31] W. Jang, K. Kim, B. G. Kim, J.-S. Nam, I.l Jeon, D. H. Wang, *Adv. Funct. Mater.* **2022**, *32*, 2207713.
[32] K. Qiao, Y. Cao, X. Yang, J. Khan, H. Deng, J. Zhang, U. Farooq, S. Yuan, H. Song, *RSC Adv.* **2017**, *7*, 52947.
[33] J. Ramade, J. Qu, A. Chu, C. Gréboval, C. Livache, N. Goubet, B. Martinez, G. Vincent, E. Lhuillier, *ACS Photonics* **2020**, *7*, 272.
[34] F. Furlan, D. Nodari, E. Palladino, E. Angela, L. Mohan, J. Briscoe, M. J. Fuchter, T. J. Macdonald, G. Grancini, M. A. McLachlan, N. Gasparini, *Adv. Opt. Mater.* **2022**, 202201816.
[35] J. Kublitski, A. Fischer, S. Xing, L. Baisinger, E. Bittrich, D. Spoltore, J. Benduhn, K. Vandewal, K. Leo, *Nat. Commun.* **2021**, *12*, 4259.
[36] Y.-Y. Yu, C.-I. Liu, Y.-C. Peng, B.-H. Jiang, Y.-W. Su, S.-J. Liu, C.-P. Chen, *Adv. Electron. Mater.* **2022**, *8*, 2200585.
[37] Y. S. Chauhan, D. D. Lu, S. Venugopalan, S. Khandelwal, J. P. Duarte, N. Paydavosi, A. Niknejad, C. Hu, *FinFET Modeling for IC Simulation and Design: Using the BSIM-CMG Standard*, Academic Press, Cambridge, MA **2015**.
[38] F. Ahmed, J. H. Dunlap, P. J. Pellechia, A. B. Greytak, *Chem. Commun.* **2021**, *57*, 8091.
[39] H. Wang, M. Desbordes, Y. Xiao, T. Kubo, K. Tada, T. Bessho, J. Nakazaki, H. Segawa, *ACS Appl. Energy Mater.* **2021**, *4*, 5918.
[40] W. Li, Y. Xu, X. Meng, Z. Xiao, R. Li, L. Jiang, L. Cui, M. Zheng, C. Liu, L. Ding, Q. Lin, *Adv. Funct. Mater.* **2019**, *29*, 1808948.
[41] M. M. Tavakoli, L. Gu, Y. Gao, C. Reckmeier, J. He, A. L. Rogach, Y. Yao, Z. Fan, *Sci. Rep.* **2015**, *5*, 14083.
[42] J. Kong, H. Wang, J. A. Röhr, Z. S. Fishman, Y. Zhou, M. Li, M. Cotlet, G. Kim, C. Karpovich, F. Antonio, N. P. Padture, A. D. Taylor, *ACS Appl. Energy Mater.* **2020**, *3*, 7231.
[43] J.-F. Wang, L. Zhu, B.-G. Zhao, Y.-L. Zhao, J. Song, X.-Q. Gu, Y.-H. Qiang, *Sci. Rep.* **2017**, *7*, 14478.
[44] W. Jang, K. Kim, B. G. Kim, J.-S. Nam, I.l Jeon, D. H. Wang, *Adv. Funct. Mater.* **2022**, *32*, 2207713.
[45] J. Liu, M. Gao, J. Kim, Z. Zhou, D. S. Chung, H. Yin, L. Ye, *Mater. Today* **2021**, *51*, 475.
[46] F. Viñes, M. Bernechea, G. Konstantatos, F. Illas, *Phys. Rev. B* **2016**, *94*, 235203.
[47] Y.-T. Huang, S. R. Kavanagh, M. Righetto, M. Rusu, I. Levine, T. Unold, S. J. Zelewski, A. J. Sneyd, K. Zhang, L. Dai, A. J. Britton, J. Ye, J. Julin, M. Napari, Z. Zhang, J. Xiao, M. Laitinen, L. Torrente-Murciano, S. D. Stranks, A. Rao, L. M. Herz, D. O. Scanlon, A. Walsh, R. L. Z. Hoye, *Nat. Commun.* **2022**, *13*, 4960.
[48] S. L. Diedenhofen, M. Bernechea, K. M. Felter, F. C. Grozema, L. D. A. Siebbeles, *Sol. RRL* **2019**, *3*, 1900075.
[49] F. Yao, L. Jiang, Y. Qi, R. Li, Y. Li, Y. Xu, H. Liu, Q. Lin, *Appl. Mater. Today* **2022**, *26*, 101262.
[50] F. P. García De Arquer, A. Armin, P. Meredith, E. H. Sargent, *Nat. Rev. Mater.* **2017**, *2*, 16100.
[51] E. Shirzadi, N. Tappy, F. Ansari, M. K. Nazeeruddin, A. Hagfeldt, P. J. Dyson, *Adv. Sci.* **2022**, *9*, 2103729.
[52] A. J. Barker, A. Sadhanala, F. Deschler, M. Gandini, S. P. Senanayak, P. M. Pearce, E. Mosconi, A. J. Pearson, Y. Wu, A. R. Srimath Kandada, T. Leijtens, F. De Angelis, S. E. Dutton, A. Petrozza, R. H. Friend, *ACS Energy Lett.* **2017**, *2*, 1416.
[53] Y. Zhang, M. Vafaie, J. Xu, J. M. Pina, P. Xia, A. M. Najarian, O. Atan, M. Imran, K. Xie, S. Hoogland, E. H. Sargent, *Adv. Mater.* **2022**, *34*, 2206884.
[54] D. Li, H. Wu, H.-C. Cheng, G. Wang, Y. Huang, X. Duan, *ACS Nano* **2016**, *10*, 6933.
[55] C. Eames, J. M. Frost, P. R. F. Barnes, B. C. O'regan, A. Walsh, M. S. Islam, *Nat. Commun.* **2015**, *6*, 7497.
[56] Z. Li, S. P. Senanayak, L. Dai, G. Kusch, R. Shivanna, Y. Zhang, D. Pradhan, J. Ye, Y.-T. Huang, H. Sirringhaus, R. A. Oliver, N. C. Greenham, R. H. Friend, R. L. Z. Hoye, *Adv. Funct. Mater.* **2021**, *31*, 2104981.
[57] F. So, Q. Dong, J. Mendes, L. Lei, D. Seyitliyev, L. Zhu, S. He, K. Gundogdu, *ACS Appl. Mater. Interfaces* **2020**, *12*, 48845.
[58] J. Zhao, Y. Deng, H. Wei, X. Zheng, Z. Yu, Y. Shao, J. E. Shield, J. Huang, *Sci. Adv.* **2017**, *3*, eaao5616.
[59] Y. Yuan, J. Huang, *Acc. Chem. Res.* **2016**, *49*, 286.
[60] Y. Zhang, M. Vafaie, J. Xu, J. M. Pina, P. Xia, A. M. Najarian, O. Atan, M. Imran, K. Xie, S. Hoogland, E. H. Sargent, *Adv. Mater.* **2022**, *34*, 2206884.
[61] R. L. Z. Hoye, B. Ehrler, M. L. Böhm, D. Muñoz-Rojas, R. M. Altamimi, A. Y. Alyamani, Y. Vaynzof, A. Sadhanala, G. Ercolano, N. C. Greenham, R. H. Friend, J. L. Macmanus-Driscoll, K. P. Musselman, *Adv. Energy Mater.* **2014**, *4*, 1301544.
[62] Y. Chu, Y. Chen, J. Zhou, B. Zhou, J. Huang, *ACS Appl. Mater. Interfaces* **2019**, *11*, 14510.

© 2023 The Authors. Small published by Wiley-VCH GmbH

16136829, 2024, 18, Downloaded from https://onlinelibrary.wiley.com/doi/10.1002/smll.202310199 by Helmholtz-Zentrum Berlin Für, Wiley Online Library on [28/04/2025]. See the Terms and Conditions (https://onlinelibrary.wiley.com/terms-and-conditions) on Wiley Online Library for rules of use; OA articles are governed by the applicable Creative Commons License